A new iterative identification algorithm for estimating the LuGre friction model parameters

Saeed Mahmoudkhani, Johnathan Gorenstein, and Keivan Ahmadi

A new iterative identification algorithm for estimating the LuGre friction model parameters

Saeed Mahmoudkhani[a,*], Johnathan Gorenstein[b], Keivan Ahmadi[b]

[a] *Faculty of New Technologies and Aerospace Engineering, Shahid Beheshti University, Tehran, Iran*
[b] *Department of Mechanical Engineering, University of Victoria, Victoria, British Columbia, Canada V8W 2Y2.*

Abstract

The parameters of dynamic friction models like the LuGre model are commonly identified by computationally intensive nonlinear optimization methods. In this paper, an alternative least-square-based iterative algorithm is proposed to simultaneously identify the LuGre model parameters and the inertial properties from a limited set of measurements. The LuGre model, expressed in two forms allowed independent identification of the static and dynamic parameters. Moreover, since the method uses response-input time-history instead of numerous constant velocity experiments (CVEs), both the inertial and friction parameters can be identified in much fewer experiments (theoretically one). A variant of the Sparse Identification of Nonlinear Dynamics method called SR3 is embedded in the algorithm to capture the nonlinear viscous friction and Stribeck effects in the friction model. Application of the algorithm to an industrial robot joint shows that the convergence of the algorithm is fast and the identified model is accurate in predicting the joint's dynamics in a wide range of velocities. The friction-velocity curves resulting from the identified model are compared to those obtained by traditional CVEs to confirm the accuracy of the identified model.

Keywords: LuGre friction model, Sparse regression, SINDy-SR3

1. Introduction

Friction modeling is essential in developing the dynamic model of multi-body mechanical systems with relative motion between components. These dynamic models are needed in various engineering applications such as model-based control of robots and machine tools, design and analysis of friction dampers used for vibration suppression of turbomachinery blades, earthquake protection of buildings, and so on.

Friction is the result of interactions between the microscopic asperities of surfaces in contact [1, 2]. Accurate physics-based modeling of friction requires

*Corresponding author

accounting for a large population of microscopic asperities and different sources of the tangential forces that would give rise to the friction force. Such a computationally intensive approach is not suitable for applications where the friction needs to be computed in real time [1, 3]. Instead, such applications commonly use empirical models of friction, which can be classified into static and dynamic models [4, 5]. Static models describe the friction in the gross sliding motion by explicitly relating the friction force or torque to the relative velocity. The most common of this class of models account for the Coulomb, viscous, and Stribeck friction effects, which give promising results in most applications where only the sliding motion is considered [6]. Parameters such as position, normal contact force, and temperature can also be included in static friction models [7–10]. Due to the simple and explicit form of static friction models, the experimental identification of their parameters is less challenging. Difficulties may nonetheless arise in collecting the required experimental data and estimating the non-linear parameters in the chosen model. A common experimental procedure moves the system at constant velocity, thus removing inertial forces, allowing direct measurement of friction in some applications [7, 11–13]. In this paper, this procedure is referred to as a constant-velocity experiment (CVE). The drawbacks of this approach are that the velocity levels are discrete and the procedure is tedious and time consuming. Additionally, precise velocity regulation is required to obtain a steady velocity throughout the experiments and the collected data must be post-processed before ready for identification. To address these drawbacks, Hensen et al. [14] presented the extended Kalman filter approach which uses a single trajectory to identify the static friction model. Other system identification methods based on general nonlinear regression and the Sparse Identification of Nonlinear Dynamics (SINDy) have also been applied in [15] with the main goal of assessing the capability of the SINDy method in friction identification. SINDy is a data-driven method recently developed by Brunton et al. [16] for the discovery of governing equations in nonlinear dynamical systems. The method is based on the sparsity-promoting regression technique and is shown to be capable of efficiently discovering interpretable and parsimonious models using small amount of data [17].

Although moving parts of mechanical systems operate mostly in their sliding regime of motion, when the motion starts or changes direction behaviors such as stick-slip motion, frictional lag, pre-sliding displacement, and hysteresis effects are present [5, 18, 19]. Most promising dynamic models incorporate additional internal states that evolve in time according to their own ordinary differential equations. Pioneering variants of these types of models are the Dahl [20] and the LuGre models [18], which have been improved over time giving rise to models such as the Leuven model [21], Generalized Maxwell-Slip (GMS) model [22], and elasto-plastic models [3, 23]. More details about different models and their properties and issues are provided in [24] and [3]. Difficulties in either numerically solving the model or the parameter identification process could be intensified in more sophisticated models.

Among the dynamic models of friction, the LuGre model is shown to predict a wide range of friction behaviors with fewer parameters compared to the

more recently proposed models [19, 25–28]. Because of this simplicity, LuGre is often the preferred model, especially in the controls community. The model has nonlinear parameters and evaluation requires integrating an additional differential equation at each time step. Identifying the parameters of the model requires a complex experimental procedure and intensive computations. This problem is evident in a commonly used identification method (IDM) introduced by De Wit and Lischinsky [29]. The process first estimates the static parameters of the model using the friction-velocity curve obtained by several closed loop CVEs. Next, the estimated parameters are used in the differential equation of the model, which has to be integrated together with the equations of motion to obtain the simulated results. The norm of the difference between the predicted and experimental data is then minimized using a nonlinear optimization algorithm (OPA) to obtain the two dynamic parameters of the model. The experimental data used in the second stage of the process is a response-input time history obtained by an open loop experiment which contains reversal and stick-slip motions. Another method is also used in [30] and [31] where, similar to [29], the static parameters are first estimated by fitting the Stribeck static model to the curve obtained by CVEs. The dynamic parameters are then estimated by exciting the system in the pre-sliding regime. In an attempt to simplify the experimental procedure, Hensen et al. [32] linearized the LuGre friction model and proposed a frequency domain IDM that only requires a single trajectory. Another method based on a single trajectory is suggested by Rizos and Fassois [33], which consists of a two-phase hybrid OPA. In the first phase, a pre-optimization using the Genetic Algorithm is performed to determine the range of parameters that include local or global minima. Next, a fine-optimization is performed using the Nelder-Mead Downhill Simplex algorithm to determine the exact location of minima. The same method is extended in [34] with the NARX model and recurrent neural networks. Different OPAs are also employed in other studies for estimating the LuGre parameters [13, 25–27, 29, 35–39].

In all the studies mentioned above, the main focus was on the estimation of the friction model parameters, while the other properties of the system like the inertial properties were assumed to be known. The only exception is the frequency-domain method in [32] which identifies the inertial and friction parameters together. There is also a class of identification procedures where all the inertial and friction parameters are estimated simultaneously. These methods include least-square method (LSQM), maximum-likelihood approach, and Instrumental Variable technique [40–42]. However, most of these studies use simpler static friction models in the identification process [25].

This study proposes a new iterative algorithm for the simultaneous identification of the inertial properties and the LuGre friction model parameters. The method only requires response-input time histories, eliminating the need of CVEs to obtain the static friction parameters. The first step of the algorithm obtains the most parsimonious and generalizable model structure to describe static friction using the SINDy sparse relaxed regularized regression (SR3) algorithm [43]. The SR3 variant of SINDy adds a relaxation factor to improve the performance on noisy datasets and outliers[43, 44]. Moreover, the partial

OPA embedded in SR3 enables the identification of models that are nonlinear in parameters [44]. This capability of SR3 is also exploited in the presented algorithm to expand the types of nonlinearities that could be included in the friction model. The result of the first step is then used in the iterative second and third steps of the algorithm to update the static parameters and identify the dynamic parameters of the LuGre model. These steps use different forms of the LuGre model with the LSQM for estimating the parameters. The internal state of the model is computed in the third step by numerically solving the LuGre differential equation. The proposed method is applied experimentally to identify the model parameters of a robot joint. The accuracy of the identified friction model is verified by comparing its predictions of friction-velocity curves against CVE results. Furthermore, the accuracy of the whole identified dynamic model of the system is confirmed by comparing the estimated torque, position and velocity time histories with the experimental results.

The dynamic model of the considered robot joint and the two interchangeable forms of LuGre friction model are explained in the next section. The various components of the proposed parameter estimation method are introduced in Section 3, which includes brief descriptions of SINDy and SR3 algorithms and the adopted function libraries. The new identification algorithm is presented in Section 4, followed by a description of the associated experimental procedure in Section 5. This section also explains the CVE method, as these results are used to validate the new IDM. Section 6 provides a general description of Akaike information criterion (AIC) and how it is used for model selection in the presented method. The presented method is implemented experimentally to identify the parameters of a robot joint's model and the results are discussed in Section 7.

2. Joint Dynamics Model

Without loss of generality, this work assumes a revolute joint. The general equation of motion for a single robotic joint, while all other joints are locked, is expressed as follows:

$$I_{zz}\frac{\mathrm{d}^2}{\mathrm{d}t^2}q\left(t\right)+mg\ C_x\ \cos\left(q\right)-mgC_y\ \sin\left(q\right)+\tau_f=\tau \tag{1}$$

where $q(t)$ denotes the joint's rotation around its axis. I_{zz} is the augmented link inertia defined by $I_{zz}=I_rN^2+\bar{I}_{zz}$, with $\bar{I}_{zz}$, I_r, and N being the link inertia, rotor inertia, and the gear ratio of the joint, respectively. Also, m is the link mass, and C_x and C_y are the center of mass coordinates with respect to a local frame located at the joint with its x-axis lying on the link axis. The actuation torque and the joint friction are denoted by τ and τ_f, respectively.

All the inertial parameters and the friction torque in Eq. (1) are identified using the IDM developed in this study. The friction torque is modeled by the

LuGre dynamic friction model, as follows [18]:

$$\tau_f = \sigma_0 z + \sigma_1 \dot{z} + \tau_v(\dot{q}) \tag{2}$$

with

$$\dot{z} = \dot{q}\left[1 - \frac{\sigma_0 z\,\mathrm{sign}(\dot{q})}{g(\dot{q})}\right] \tag{3}$$

where σ_0 and σ_1 are the dynamic parameters of the LuGre model, representing respectively the stiffness and damping of the microscopic elastic bristles in the contact surface. The viscous component of the friction torque is denoted by $\tau_v(\dot{q})$ and z is the non-measurable internal state of the model, representing the average deflection of the bristles. This parameter can only be determined by solving the nonlinear ordinary differential equation in Eq.(3). The $g(\dot{q})$ term in Eq.(3) is defined according to the steady-state (static) friction by setting $\dot{z}$ in Eqs. (2) and (3) equal to zero, which gives the following:

$$\tau_{Sf} = \mathrm{sign}(\dot{q})g(\dot{q}) + \tau_v(\dot{q}) \tag{4}$$

Comparing Eq.(4) with common Stribeck friction models in the literature for the sliding regime of motion (see e.g. [6, 45]), one can deduce that $g(\dot{q})$ includes the Coulomb friction and the Stribeck effects. Different functions have been introduced in literature for describing $g(\dot{q})$, but the most common one is the following [19]:

$$g(\dot{q}) = \left(f_c + (f_s - f_c)\, e^{-\left|\frac{\dot{q}}{\Omega_s}\right|^{\delta}}\right) \tag{5}$$

where f_c and f_s are the Coulomb and static friction terms respectively, Ω_s is the Stribeck velocity, and δ is an additional constant parameter.

Solving for z from Eq. (3) and substituting the result into Eq. (2) results in the following alternative form of the LuGre model:

$$\tau_f = \mathrm{sign}(\dot{q})\left(1 - \frac{\dot{z}}{\dot{q}}\right) g(\dot{q}) + \sigma_1 \dot{z} + \tau_v(\dot{q}) \tag{6}$$

Both of the interchangeable forms of the LuGre model, Eq. (2) and Eq. (6), will be used in the presented identification process.

3. Parameter estimation method

The parameter estimation method used in the proposed identification algorithm is generally based on the implicit-SINDy method. Particularly, in the first step of the proposed algorithm, we exploit the sparsity-promoting capability of SINDy-SR3 to detect the parsimonious set of functions that efficiently describe the static friction torque. Then, in two subsequent steps, the same SR3 algorithm without sparsification is used to estimate the dynamic parameters and modify the identified static friction parameters. In the rest of this

section, the implicit-SINDy and SR3 algorithms are described, followed by an introduction of the corresponding candidate functions used in the parameter estimation process.

3.1. Implicit-SINDy

All variants of the SINDy method require the equation of motion to be formulated in state-space form. In the original form of SINDy, the equations of motion are written in the standard state-space form, where the time derivative of the state is expressed as a weighted sum of the candidate functions. In implicit-SINDy [46, 47], the implicit state-space form is used, where the adopted functions depend on both the state and its first-order derivative. The same approach is used here, but applied to the second-order equation of motion. Moreover, the candidate functions are assumed to depend non-linearly on a set of additional parameters denoted by $\boldsymbol{\alpha}$. With these considerations, the following system of linear algebraic equations is formed to relate the applied rotor torque to the resulting joint motion:

$$\boldsymbol{\Theta}(\mathbf{Q}, \dot{\mathbf{Q}}, \ddot{\mathbf{Q}}, \boldsymbol{\alpha})\boldsymbol{\xi} = \boldsymbol{\tau} \tag{7}$$

where $\boldsymbol{\xi}$ is the coefficient vector, which is assumed to be sparse, $\mathbf{Q}$ is the column vector of rotation angles sampled at n instants of time, and arranged as, $\mathbf{Q} = [q_1, ..., q_n]^T$ with $q_i = q(t_i)$, and $\boldsymbol{\tau}$ is the column vector of the rotor torque values measured at the same time instants. $\boldsymbol{\Theta}$ is the matrix of candidate functions. Each column of $\boldsymbol{\Theta}$ corresponds to the numerical values of each candidate function at different time instants. Denoting the kth candidate function by F_k, $\boldsymbol{\Theta}$ would be constructed as follows:

$$\boldsymbol{\Theta} = \begin{bmatrix} F_1(q_1, \dot{q}_1, \ddot{q}_1, \alpha) & \cdots & F_r(q_1, \dot{q}_1, \ddot{q}_1, \boldsymbol{\alpha}) \\ \vdots & \ddots & \vdots \\ F_1(q_n, \dot{q}_n, \ddot{q}_n, \boldsymbol{\alpha}) & \cdots & F_r(q_n, \dot{q}_n, \ddot{q}_n, \boldsymbol{\alpha}) \end{bmatrix} \tag{8}$$

with r being the total number of considered candidate functions. The identification of the nonlinear parameters, $\boldsymbol{\alpha}$, requires an additional optimization process that can be efficiently completed using the SINDy-SR3 method [44].

3.2. SR3 algorithm

The SR3 method solves the following optimization problem to find a sparse solution for Eq. (7) [44]:

$$\min_{\xi, \mathbf{W}} \frac{1}{2} \left\| \boldsymbol{\Theta}(\mathbf{Q}, \dot{\mathbf{Q}}, \ddot{\mathbf{Q}}, \boldsymbol{\alpha})\boldsymbol{\xi} - \boldsymbol{\tau} \right\|^2 + \lambda R(\mathbf{W}) + \frac{1}{2\nu} \|\boldsymbol{\xi} - \mathbf{W}\|^2, \tag{9}$$

where $\mathbf{W}$ is an auxiliary vector introduced to relax the optimization, and R is taken as the ℓ_0 norm according to [44]. λ and ν denote regularization and relaxation parameters, respectively. These parameters are adjusted to obtain a parsimonious solution. Larger values of λ lead to a more sparse solution and by

lowering the value of ν, $\mathbf{W}$ approaches $\boldsymbol{\xi}$. The solution of (9) can be obtained by implementing the following procedure:

1. Set initial values for the components of $\boldsymbol{\alpha}$ and the vector $\mathbf{W}$ (a zero vector is usually a proper starting point for $\mathbf{W}$). Also set λ and ν values.
2. Solve the optimization problem, $\min_{\boldsymbol{\xi},\,\mathbf{W}} \frac{1}{2}{E_\tau}^2 + \frac{1}{2\nu}\|\boldsymbol{\xi} - \mathbf{W}\|^2$, where E_τ is the ℓ_2 norm of the error in torque prediction, defined as, $E_\tau = \left\|\boldsymbol{\Theta}(\mathbf{Q}, \dot{\mathbf{Q}}, \ddot{\mathbf{Q}}, \boldsymbol{\alpha})\xi - \boldsymbol{\tau}\right\|$. The solution to this optimization problem can be readily obtained by using the least-square method, giving the following solution for $\boldsymbol{\xi}$:

$$\boldsymbol{\xi} = \left(\Theta^{\mathrm{T}}\Theta + \frac{1}{\nu}\mathbf{I}\right)^{-1}(\Theta^{\mathrm{T}}\boldsymbol{\tau} + \frac{1}{\nu}\mathbf{W}) \tag{10}$$

   where $\mathbf{I}$ is the identity matrix of the same dimension as the coefficient vector, $\boldsymbol{\xi}$.
3. Update $\mathbf{W}$ to $\mathbf{W} = \mathrm{prox}_{\nu\lambda R}(\boldsymbol{\xi})$, where the proximity operator, $\mathrm{prox}_{\nu\lambda \mathrm{R}}(\boldsymbol{\xi})$, for $R = \ell_0$, sets all the elements of $\boldsymbol{\xi}$ that are smaller than $\sqrt{(2\nu\lambda)}$ to zero [43].
4. Check if $\mathbf{W}$ has converged. If so, continue to the next step. Otherwise, repeat steps 2 and 3.
5. Minimize ${E_\tau}^2$ by setting the gradient of the function with respect to $\boldsymbol{\alpha}$ to zero. The following set of nonlinear algebraic equations in $\boldsymbol{\alpha}$ are solved by the Newton-Raphson method. This numerical solution requires computing the gradient and the Hessian of the equations, defined as follows:

$$\begin{aligned} \mathbf{g} &= \nabla_\alpha \left(\left\|\boldsymbol{\Theta}(\mathbf{Q}, \dot{\mathbf{Q}}, \ddot{\mathbf{Q}}, \alpha)\boldsymbol{\xi} - \boldsymbol{\tau}\right\|^2\right) \\ \mathbf{H} &= \nabla_\alpha^2 \left(\left\|\boldsymbol{\Theta}(\mathbf{Q}, \dot{\mathbf{Q}}, \ddot{\mathbf{Q}}, \boldsymbol{\alpha})\boldsymbol{\xi} - \boldsymbol{\tau}\right\|^2\right) \end{aligned} \tag{11}$$

   By using the definition of the ℓ_2 norm, the components of the Hessian matrix and gradient vector are determined as follows:

$$\begin{aligned} g_i &= \sum_{k=1}^{n} \left[(\boldsymbol{\Theta}\boldsymbol{\xi})_k - \tau_k\right]\left(\frac{\partial \boldsymbol{\Theta}}{\partial \alpha_i}\boldsymbol{\xi}\right)_k \\ H_{ij} &= \sum_{k=1}^{n} \left[(\boldsymbol{\Theta}\boldsymbol{\xi})_k - \tau_k\right]\left(\frac{\partial^2 \boldsymbol{\Theta}}{\partial \alpha_i \partial \alpha_j}\boldsymbol{\xi}\right)_k + \sum_{k=1}^{n}\left(\frac{\partial \boldsymbol{\Theta}}{\partial \alpha_i}\boldsymbol{\xi}\right)_k\left(\frac{\partial \boldsymbol{\Theta}}{\partial \alpha_j}\boldsymbol{\xi}\right)_k \end{aligned} \quad i = 1..n_p \tag{12}$$

   where n_p is the number of nonlinear parameters in $\boldsymbol{\alpha}$. Now, the new value of $\boldsymbol{\alpha}$ can be updated to $\boldsymbol{\alpha} - \mathbf{H}^{-1}\mathbf{g}$. Continue updating until all the entries in $\boldsymbol{\alpha}$ converge to the final value. It should be noted that because this procedure only gives local minima for $\boldsymbol{\alpha}$, the process has to be repeated for different initial values of $\boldsymbol{\alpha}$. This repetition can make the process cumbersome, especially if there are many of these nonlinear parameters [44].
6. Calculate the norm of the difference between $\boldsymbol{\alpha}$ and its value in the previous iteration. If the calculated value is not sufficiently small, go to step

2 and repeat the whole process until convergence is reached.

The above algorithm determines the active candidate functions in the first step of the proposed IDM. The coefficients ($\boldsymbol{\xi}$) of the remaining active functions are then determined at the end of the SR3 algorithm by the least-square method [44]. In the remaining second and third steps of the proposed IDM, λ is set to zero, which makes the SR3 algorithm equivalent to the LSQM with relaxation. The relaxation term improves the condition number of the matrix and thereby the accuracy of the matrix inversion needed in the least-square method [43].

3.3. The adopted candidate functions

Theoretically, any arbitrary function can be included in the library of candidate functions [16]; however, when possible, it is recommended to choose the functions based on the prior knowledge of the system's physics. Hence, it is reasonable here to use the same functions appearing in the equation of motion, i.e. Eq.(1). The first three basis functions are then defined as follows:

$$F_{1,2,3} = [\ddot{q}, \cos(q), \sin(q)] \tag{13}$$

The above functions are used only in step 1 and the first iteration of step 2 in the proposed algorithm (see Section 4). Moreover, the coefficients obtained for each of these functions at the first step will not be updated during the remaining part of the identification process. These coefficients represent the inertial properties, I_{zz}, $mg\,C_x$, and mgC_y, and thus the part of the equation of motion corresponding to the first three terms on the left-hand-side of Eq. (1) will be considered as known in the whole process after the first iteration of step 2. Hence, τ in Eq. (9) would be replaced by $\tau - I_{zz}\ddot{q}\,(t) + mg\,C_x\,\cos\,(q) - mgC_y\,\sin\,(q)$. Different candidate functions are adopted to describe friction at each step of the proposed IDM, as explained separately in the following two subsections.

3.3.1. Candidate functions for the static friction model

Assuming that viscous friction can be described by power series, $\tau_v = \sum_{i=1}^{n_v} c_{vi}\dot{q}^i$, the following basis functions are also added to the library of candidate functions:

$$F_{4,5,\ldots,3+n_v} = [\dot{q}, \dot{q}^2, ..., \dot{q}^{n_v}] \tag{14}$$

where n_v is a positive integer number of viscous terms. Additionally, the following set of candidate functions are used to account for Coulomb and Stribeck friction terms:

$$F_{4+n_v\ldots5+n_v+n_s} = \text{sign}(\dot{q})\left[1, e^{-\left|\frac{\dot{q}}{\Omega_s}\right|^{\delta_1}}, e^{-\left|\frac{\dot{q}}{\Omega_s}\right|^{\delta_2}}, ..., e^{-\left|\frac{\dot{q}}{\Omega_s}\right|^{\delta_{n_s}}}\right] \tag{15}$$

where n_s is the number of exponential functions included in the function library and Ω_s will be determined using the Newton method incorporated in the SR3 algorithm presented in Section 3.2. Consequently, the vector of nonlinear

parameters denoted by $\boldsymbol{\alpha}$ in Eq. (7) has a single component, Ω_s. The rest of the nonlinear parameters, δ_i's, are given a set of values between 0.5 and 4, which is consistent with the range of estimations found in most studies. It is possible to consider δ as an additional nonlinear parameter and run the SR3 algorithm for both Ω_s and δ. However, SR3's gradient-based optimization is more likely to find a local, rather than global, minimum with the additional nonlinear parameter.

3.3.2. Candidate functions for the dynamic friction model

The candidate functions to represent viscous friction at the second and third steps include those terms in Eq. (14) that are still active at the end of the first step of the algorithm. In addition to those, to properly capture the friction behaviour at lower velocities, the following functions are introduced in the second step:

$$F_{4+n_v\ldots6+n_v+\bar{n}_s} = \text{sign}(\dot{q}) \left[1, \dot{z}, \left(1-\frac{\dot{z}}{\dot{q}}\right) e^{-\left|\frac{\dot{q}}{\Omega_s}\right|^{\delta_i}}, \left(1-\frac{\dot{z}}{\dot{q}}\right) e^{-\left|\frac{\dot{q}}{\Omega_s}\right|^{\delta_j}}, ..., \left(1-\frac{\dot{z}}{\dot{q}}\right) e^{-\left|\frac{\dot{q}}{\Omega_s}\right|^{\delta_k}}\right] \tag{16}$$

where i, j, and k are the integer numbers between 1 and n_s that are found to be effective at the end of the first step and $\bar{n}_s$ is the total number of effective exponential functions. At each iteration of step 2, $\dot{z}$ in Eq. (16) is determined at the preceding iteration of step 3.

In the third step, the alternative form of the dynamic friction model presented in Eq. (2) is used, yielding the following candidate functions:

$$F_{4+n_v\ldots6+n_v} = [u, \dot{u}], \tag{17}$$

where $u = \sigma_0 z$, which has the same units as the applied torque.

4. Proposed iterative identification algorithm

The flowchart of the presented algorithm is shown in Fig. 1. The identification process consists of three major steps, each step executing the SR3 algorithm with a different library of functions, as described in Section 3.

In the first step, the model structure is determined by running the SR3 algorithm for different values of λ and selecting the structure with the lowest AIC value. The selected model structure will be a compromise between prediction error and number of active terms. The selected model is then used in the second and third steps. Step 1 also identifies the first approximation of the static friction model parameters.

Steps 2 and 3 form parts of the outer and inner iteration loops, respectively, shown in Fig.1. In each iteration of step 2, the coefficients of the active terms in Eq.(14) and Eq. (16) are determined. The first iteration of step 2 includes the inertial functions (Eq. (13)) and starts with $\dot{z}$ equal to zero. Subsequently, this step provides an estimate of $g(\dot{q})$ to step 3.

Step 3, an inner iterative loop built into step 2, starts with numerically solving Eq. (3) for z while $\dot{q}$ is taken from the measured velocity vector and σ_0 is assigned or obtained from the iteration of step 2. Next, the SR3 algorithm is formulated using the library functions given in Eq. (17) as well as the active viscous terms, with τ replaced by $\tau - I_{zz}\ddot{q}(t) + mg\, C_x \cos(q) - mgC_y \sin(q)$. SR3 computes the coefficients of the functions u and $\dot{u}$, which are used to determine σ_1 and update σ_0. According to Eqs. (2) and (17), the coefficient of the function $u(= \sigma_0 z)$ should be equal to unity, however, this would only happen if σ_0 converges. Hence, as long as the coefficient of u (denoted by ξ_u) is far from unity, we must continue updating σ_0 in the inner loop of the process using the following relationship:

$$\sigma_0^{new} = \sigma_0^{old} \xi_u \tag{18}$$

From Eqs. (2) and (17) it can also be deduced that the coefficient of $\dot{u}$ has to be equal to σ_1/σ_0. Therefore, σ_1 can be determined as follows:

$$\sigma_1 = \sigma_0^{new} \xi_{\dot{u}}, \tag{19}$$

where $\xi_{\dot{u}}$ is the coefficient of $\dot{u}$ obtained by applying the SR3 method. σ_0, σ_1, and z will be iteratively updated in step 3 until the training error, E_τ, starts to increase. With this stop condition, ξ_u would not necessarily approach unity at the end of the inner loop, which means that $g(\dot{q})$ needs to be recalculated through step 2 in the outer loop using the updated estimation of $\dot{z}$. This process is then repeated until $|\sigma_0^{new} - \sigma_0^{old}|$ converges.

Due to the complicated form of the proposed algorithm, its formal convergence analysis is not straightforward. However, the experimental results presented in Section 7 confirm its convergence in practice.

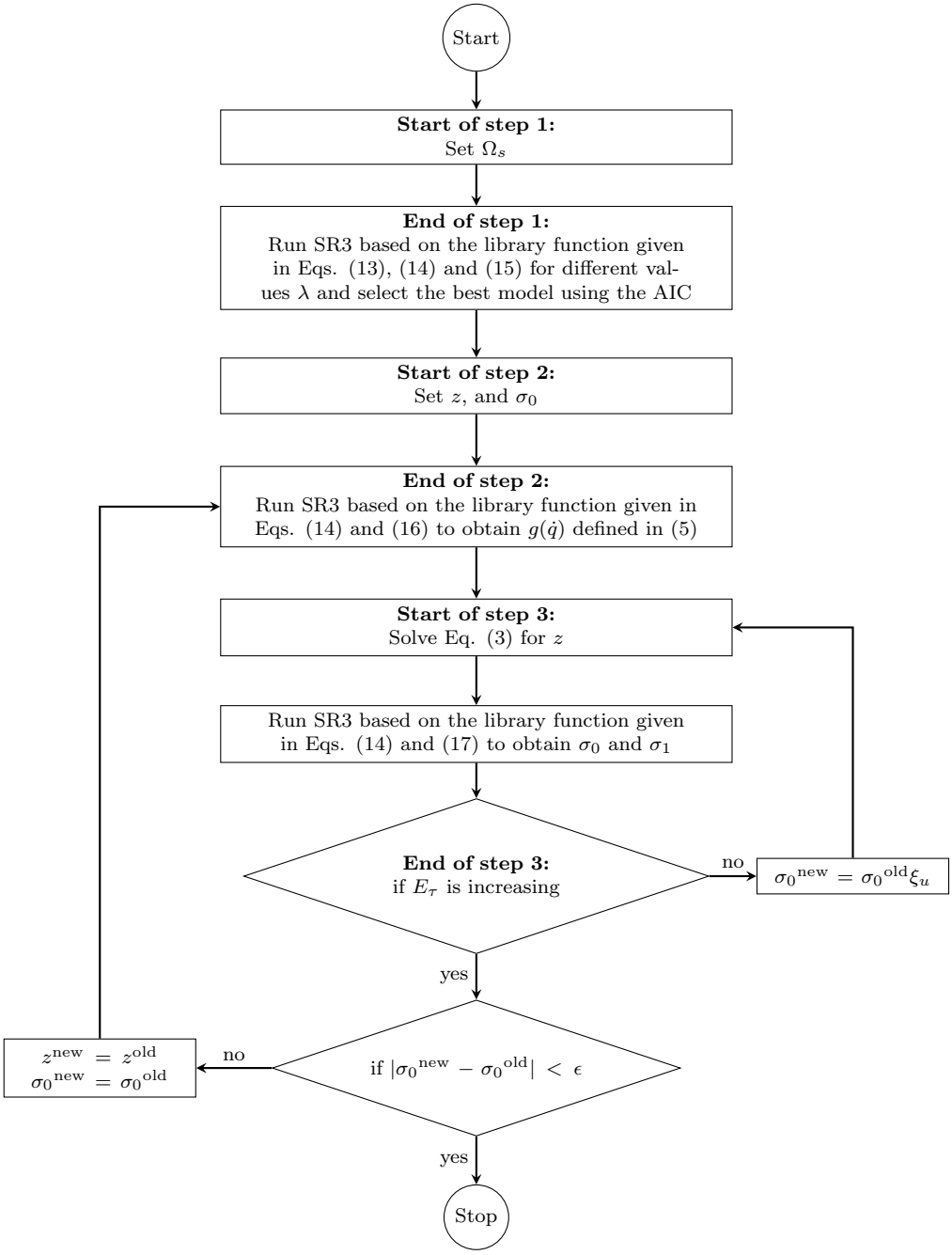

Figure 1: The flowchart of the proposed iterative identification algorithm

5. Collecting experimental data

The experimental procedure for obtaining the joint's friction torque at various velocities is presented in this section. The procedure is known as a Constant Velocity Experiment and is used to validate the performance of the proposed IDM. Next, the experimental datasets that are chosen for training, validation, and testing of the proposed IDM are described.

5.1. Constant-velocity experiments

In CVEs, the friction torque is extracted from the total actuation torque that moves the joint back and forth at a constant velocity [7, 10]. The rotor torque applied in these two opposite directions can be obtained from Eq. (1) by setting $\ddot{q} = 0$, as follows:

$$\begin{aligned} \tau^{+} &= \tau_f\left(\dot{q}\right) + \tau_g\left(q\right), \\ \tau^{-} &= \tau_f\left(-\dot{q}\right) + \tau_g\left(q\right), \end{aligned} \tag{20}$$

where τ^{+} and τ^{-} are the rotor torques in the forward and backward directions, respectively, and τ_g is the gravity torque defined by $\tau_g = mg\,C_x\,\cos\left(q\right) - mgC_y\,\sin\left(q\right)$. Assuming that the friction is direction-independent (i.e. $\tau_f(-\dot{q}) = -\tau_f(\dot{q})$), Eq. (20) can be solved to obtain the friction and gravity torques in terms of the measurable rotor torques:

$$\begin{aligned} \tau_f(\dot{q}) &= \frac{\tau^{+} - \tau^{-}}{2}, \\ \tau_g(q) &= \frac{\tau^{+} + \tau^{-}}{2}. \end{aligned} \tag{21}$$

The constant-velocity trajectories start from zero velocity at one extreme of the joint's permissible range of motion and end with zero velocity at the other extreme. This motion is then repeated in the reverse direction. A trapezoidal velocity profile is used, where changes in the robots joint velocity are done with constant acceleration. This profile is the default motion trajectory of the robot used, allowing a simple point-to-point command to be issued with the machine velocity target specified.

Figure. 2 shows the data collected from an experiment with the target velocity (TVel) of .009 rad/s. The acceleration curve in this figure was obtained by computing the second derivative of the rotation angle using the total-variation regularized difference (TVRegDiff) method [48, 49], which prevents the magnification of high-frequency noise during numerical differentiation. The regularization hyperparameter in TVRegDiff was set to 1000. Moreover, following the approach suggested by [50], instead of the original measured rotation angle, the data obtained by double-time integration of the de-noised acceleration signal is used to obtain the rotation angle in all of the training and test datasets. A similar approach was also used to compute the velocities. The position and velocity plots obtained are shown in Fig. 2 together with the raw position signal, with no considerable differences visible.

In Fig. 2(b), the measured raw torque signal is presented together with the de-noised signal obtained by first taking the time derivative of the signal using TVRegDiff and then integrating the result in time. The regularization hyperparameter of 1000 was again found to be a proper value in this case. It is evident that the measured torque is largely contaminated with noise, where a portion of it is removed by the described de-noising method. However, even after the signal is de-noised, some relatively high-frequency oscillations still remain in the signal, which is more clearly shown in Fig. 3(a). These oscillations can also be seen in the acceleration signal shown in the same figure. Attempts to remove these oscillations by using different values for the TVRegDiff hyperparameter were unsuccessful. The structural vibrations that occur due to the stick-slip phenomenon at the low-speed motion might be responsible for the high-frequency oscillations observed in the acceleration and torque signals. The results obtained for the higher TVel of 2.13 rad/s are also presented in Fig. 3(b), which show no such oscillations in the de-noised signal. This may be attributed to the faster dissipation of the stick-slip motion at the beginning and reversal points of the motion at larger velocities.

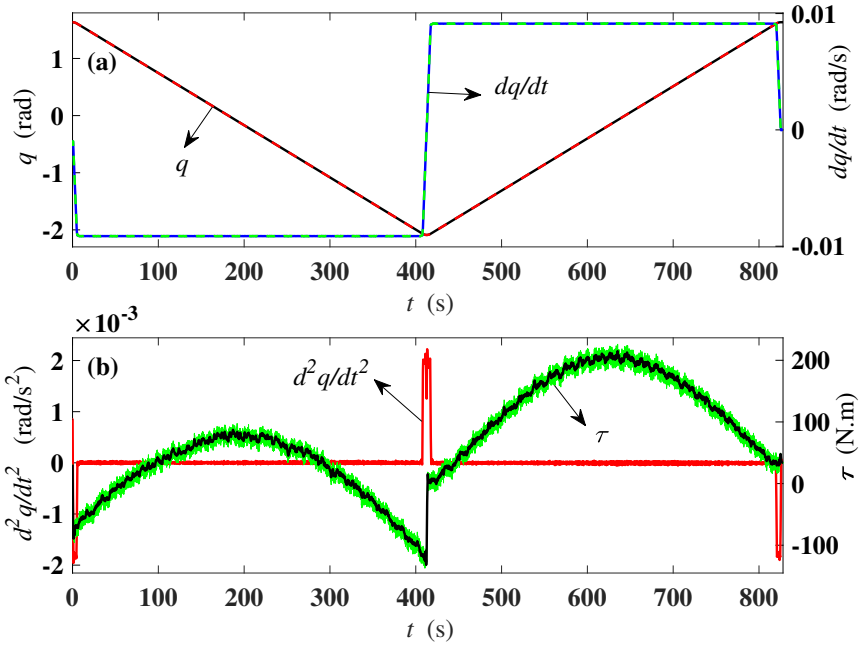

Figure 2: The results of the CVE with TVel=0.009 rad/s for (a) the angular position and velocity (Solid lines: directly de-noised signal, dashed lines: obtained by time-integration of the de-noised acceleration) (b) the rotor torque and the acceleration obtained using TVRegDiff (Thin green line: raw torque signal, thick black line: de-noised torque signal)

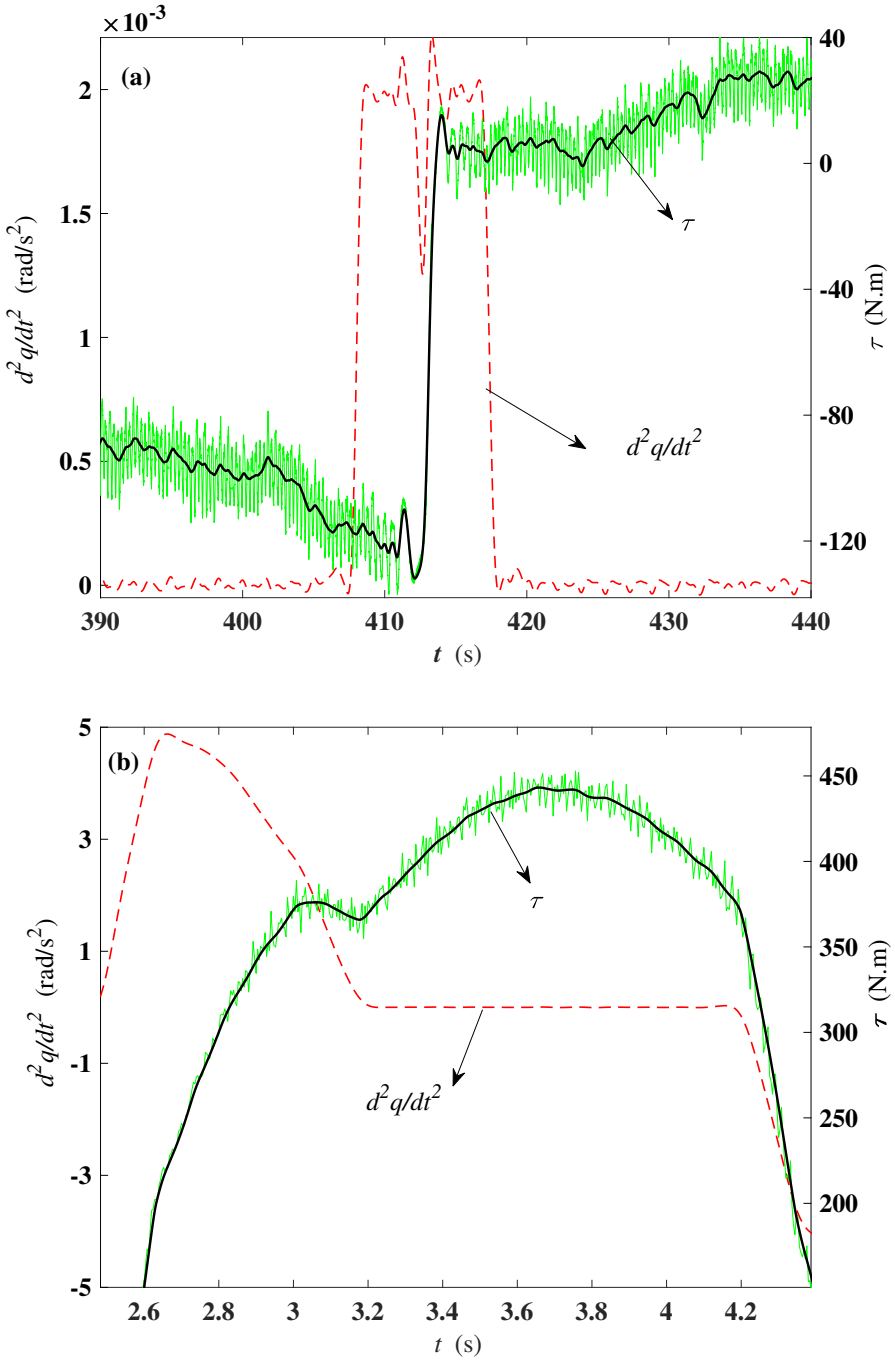

Figure 3: A zoomed view of the results obtained by CVE for (a) TVel=0.009 rad/s (b) TVel=2.13 rad/s

The next step for determining the joint friction is to extract τ^+ and τ^- from the portion of the measured signal that has negligible acceleration. To determine those points in the signal, the acceleration is assumed zero below a defined threshold. Moreover, when using Eq.(21) for computing the friction, care needs to be taken to ensure that τ^+ and τ^- correspond to the same positional range, because only then can the gravity torque be properly cancelled. Since there will be small variations in the torque computed with this method, the mean value of the resulting values is used to represent the joint friction at the tested constant velocity. The described experiment is carried out for 40 different TVels ranging from 0.009 rad/s to 2.13 rad/s; the resulting velocity-friction curve is presented in Section 7.

5.2. Preparing the data set for the proposed IDM

The proposed identification algorithm uses the time history of the applied torque and resulting joint displacement, velocity, and acceleration. Unlike the CVEs method explained in the previous section, joint velocity does not need to be kept constant in the presented method. Conversely, the trajectory needs to cover a reasonable range of velocities, including zero. Nonetheless, to be able to compare the results of the CVEs with the presented method, we use the same constant-velocity measurements here as well. This does not take away from the informativeness of the applied dataset because the acceleration and deceleration periods before or after constant velocity parts provide sufficient information about the full friction behaviour of the joint. Among the constant-velocity trajectories used in the CVEs, a reasonable choice for training the model would be the trajectories at TVel of 0.127 and 2.13 rad/s, one covering the joint's dynamics in low-speed motion and the other in high-speed. We will refer to the signals measured during the TVel 0.127 and 2.13 rad/s experiments as the training datasets 1 and 2, respectively. The signals measured at TVels 0.03 and 1.75 rad/s are used for validation. The signals measured at TVels 0.81 and 1.4 rad/s (referred to as the test data 1 and test data 2, respectively) are used for assessing the performance of the identified model.

6. Model selection

A model selection strategy needs to be adopted at the first step of the algorithm to determine the value of λ that is associated with the most parsimonious but generalisable model structure among those considered in SINDy-SR3. Akaike Information Criteria (AIC) is used in this work, where its value is minimized over the hyperparameter λ. For finite sample sizes, the AIC value is defined as follows: [51]:

$$\mathrm{AIC} = 2\,k + m \ln\left(\frac{\mathrm{RSS}}{m}\right) + 2\,\frac{(k+1)\,(k+2)}{m-k-2}, \tag{22}$$

where k is the number of free parameters; in our case, k is equal to the number of non-zero components of the coefficient vector, ξ. The variable m in Eq. (22)

is the total number of observations. Following the approach of Mangan et al. [51], the validation datasets 1 and 2 are combined and then divided into 10 equal parts, with each part being considered as a single observation. RSS in Eq. (22) represents the residual sum of squares, defined as follows [51]:

$$\mathrm{RSS} = \sum_{i=1}^{m} E_{avg}\left(\boldsymbol{\tau}^i, \boldsymbol{\tau}^{i,es}\right) \tag{23}$$

where $\boldsymbol{\tau}^i$ and $\boldsymbol{\tau}^{i,es}$ are, respectively, the experimentally measured and estimated vectors of the rotor torques for the ith observation time series. In [51], $E_{avg}\left(\boldsymbol{\tau}^i, \boldsymbol{\tau}^{i,es}\right)$ for each observation of the time-series is calculated using the following formula:

$$E_{avg}\left(\boldsymbol{\tau}^i, \boldsymbol{\tau}^{i,es}\right) = \sum_{j=1}^{n_i} \left|(\tau^i)_j - (\tau^{i,es})_j\right| \tag{24}$$

where n_i is the number of time instants in the ith observation, and $(\tau^i)_j$ and $(\tau^{i,es})_j$ are the jth component of the ith observation and estimated data, respectively. The hyperparameter, ν, in the SR3 algorithm could also be tuned based on the same model selection criteria, however, this would lead to a significantly more complex and computationally intensive model selection (curse of dimensionality). To avoid this, even in [43] wherein the SR3 method is introduced, only λ is considered in the model selection. Therefore, we set ν equal to 0.01 by comparing the relative torque estimation error resulting from a set of candidate values for ν. Finally, after calculating AIC for candidate values of λ, the model with the lowest AIC is selected as the most accurate yet generalisable model. Alternatively, by defining the relative AIC as, $\mathrm{AIC_r} = \mathrm{AIC} - \mathrm{AIC_{min}}$ with $\mathrm{AIC_{min}}$ being the minimum value of the AIC values, the best model will be the one with $\mathrm{AIC_r} = 0$.

7. Results

In this section, the results of applying the proposed model identification algorithm to joint 5 of a KUKA KR90 R3100 robot are presented. In the first subsection, the results from step 1 of the algorithm are presented, which focuses on the first approximation of the static friction model. Next, the dynamic friction model identified in the iterative part of the algorithm (i.e. steps 2 and 3) is presented and the convergence and accuracy of the method are assessed. Finally, the friction-velocity curves from the CVEs are comapred to both the dynamic and static models.

7.1. First approximation of the static model

In the first step of the algorithm, the vector $\mathbf{Q}$ measured during training tests is used to construct the matrix of the candidate functions, $\boldsymbol{\Theta}$, with columns defined in (13), (14) and (15). z is set to zero in this step to consider only the

static part of the friction model. The initial value of Ω_s is set to 0.01. Other values including .002, .005, .015 and .02 were examined as the initial value of Ω_s, but they gave larger relative errors in torque prediction. The model selection process is then carried out by running the SR3 algorithm for different values of λ, yielding the result shown in Fig. 4. In this figure, the $\mathrm{AIC_r}$ values and the number of functions that are eliminated from candidates during the sparsification process are given for different values of λ. $\mathrm{AIC_r}$ becomes zero at $\lambda = 350$, which corresponds to the model with nine active functions out of the 23 candidate functions used in $\mathbf{\Theta}$.

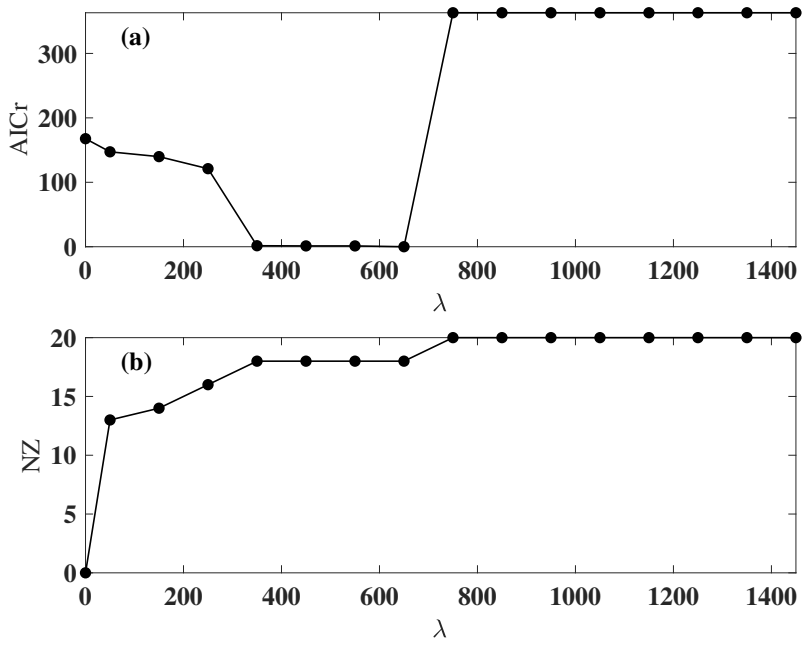

Figure 4: Variation of $\mathrm{AIC_r}$ and the number of zero terms (denoted by NZ) with λ. The figure is used to select a parsimonious static friction model

In Fig. 5, the coefficients of the adopted functions are presented. Figure 5(a) shows the coefficients of different integer powers of velocity in the viscous friction model. Only the first three odd powers are retained in this figure, signifying the nonlinearity and direction-independence of viscous friction. In Fig. 5(b), the red bar, corresponding to the zero value of δ_i, represents the Coulomb friction term, f_c. Other bars show the coefficients of $\exp(-\left|\frac{\dot{q}}{\Omega_s}\right|^{\delta_\mathrm{i}})$ with different values of δ_i, which are all zero except those with $\delta_i = 0.5$ and 2.25. Hence, the selected model consists of two exponential functions and thereby two breaks in the corresponding friction-velocity curve shown in Fig. 7. This figure also shows the friction-velocity curve resulting from the CVEs, which agrees well

with the result of the identified static model except at velocities lower than approximately 0.03 rad/s. The major discrepancies present by the identified model are the additional local minimum that appears around 0.002 rad/s and the maximum friction torque before the second break is estimated to be 10 percent less than found by the CVE.

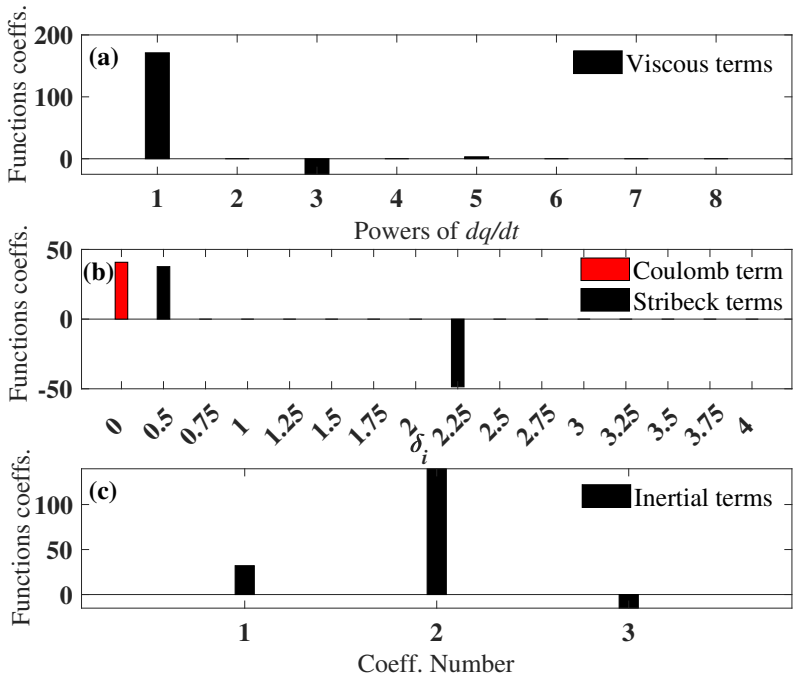

Figure 5: Numerical values of the coefficient vector components, ξ_i, corresponding to the functions given in (a) Eq. (14) for the viscous friction (b) Eq.(15) for the Coulomb and Stribeck friction (c) Eq. (13) for the inertial terms of the governing equation

A similar two-break static friction model was also found in [11], where it was speculated that two sliding motions at two different points in the drivetrain are responsible for this observation. However, such behavior has not been reported often in the literature and the common static friction models include only one exponential function that can reproduce only a single break-away point. Moreover, since the first peak in Fig. 7(a) occurs below where the CVE was possible, it is hard to confirm whether there is a physical phenomenon behind it or it is a misidentification. Therefore, in addition to the two-break model, a single-break model was obtained by replacing the function, $\text{sign}(\dot{q})$, in the friction model (Eq. (4)) with the sigmoid function, $\tanh(K\dot{q})$, where K is a constant parameter. In the following, the initial model and the modified model will be referred to as model A and B, respectively. A negative coefficient is obtained

for the exponential function when K is large, which is physically inadmissible. $\tanh(K\dot{q})$ approaches the sign function with larger values of K, yet lower values of K provide physically reasonable results and also facilitate the simulation of the equations of motion. Here, K is set to 150 and the model selection process is repeated, yielding the result in Fig. 6. It is evident from this figure that only one exponential function with $\delta_i = 0.75$ is retained in the selected model. The obtained friction-velocity curve is shown in Fig. 7(b) together with the CVE result. A good match is observed between the results at higher velocities. Moreover, there is only one local maximum in the low-velocity region, with a relative error of about 15%.

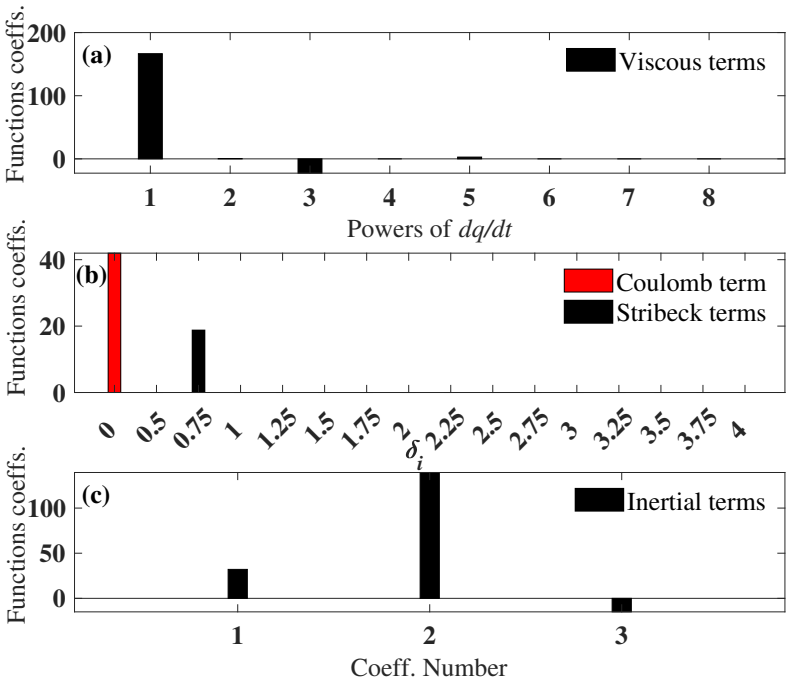

Figure 6: Numerical values of ξ_i, corresponding to the functions in Eqs. (14), (15), and (13) with $\text{sign}(\dot{q})$ replaced with $\tanh(K\dot{q})$ for (a) the viscous friction functions (b) the Coulomb and Stribeck friction functions (c) for the inertial terms of the governing equation

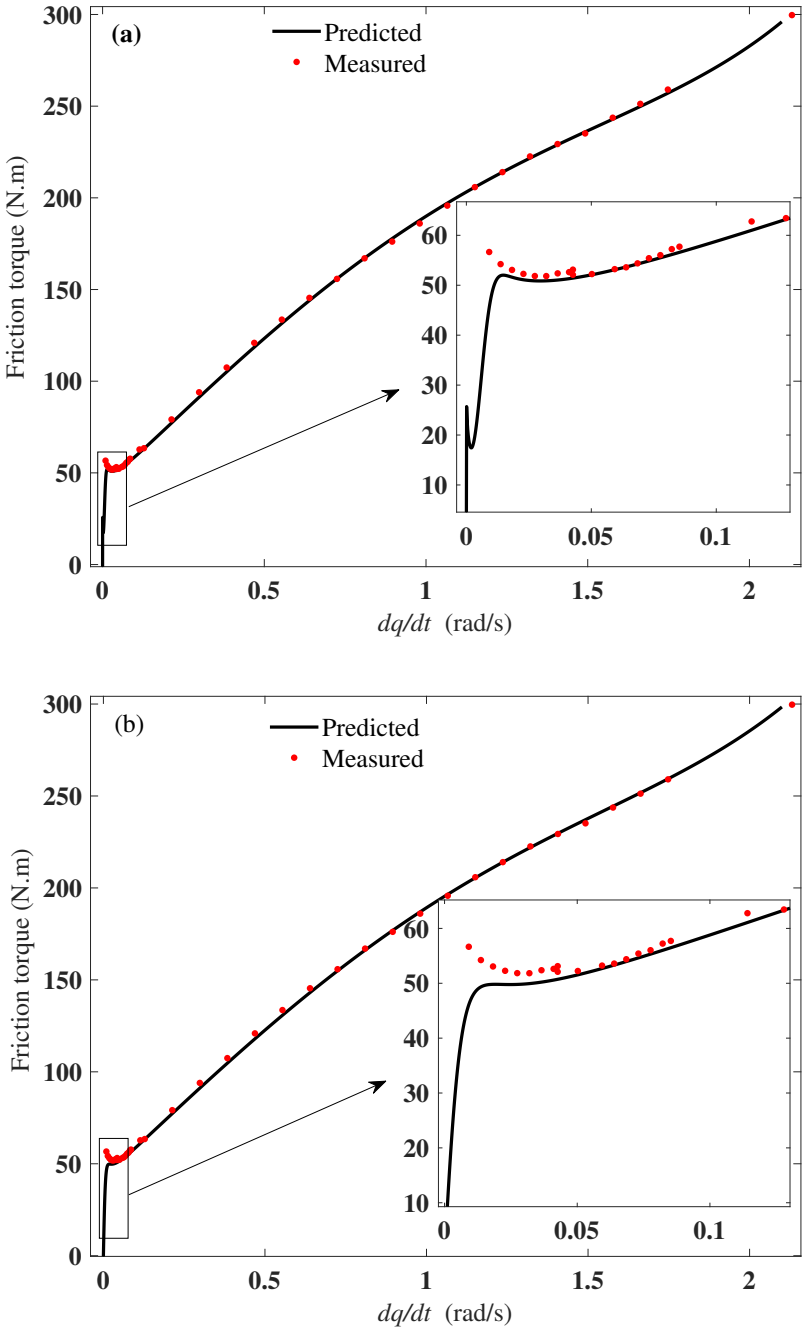

Figure 7: Comparison of the friction-velocity curve obtained by CVEs with the result of the first approximation of the static model obtained using SR3 for (a) model A (b) model B ($\text{sign}(\dot{q})$ is replaced with $\tanh(K\dot{q})$)

The time evolution of the relative torque prediction error for both model A and B are shown in Fig. 8. The torque prediction error in this figure is defined as $(\tau_j - {\tau_j}^{es})/\max(\tau_j = 1..n)$ where j represents the jth time instant and ${\tau_j}^{es}$ is the torque estimated by the static friction model. As expected, the static model is less accurate at near-zero velocities but performs well at higher velocities where viscous friction dominates.

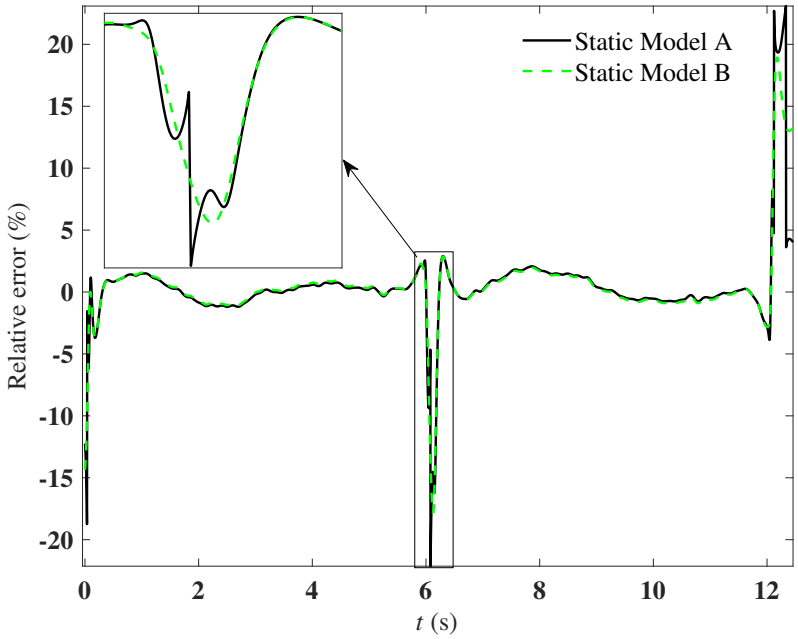

Figure 8: Comparing the time evolution of the relative error in torque, obtained by the static friction model corresponding to models A and B (The measured data is the test data set 1, and the relative error is defined by $(\tau_j - {\tau_j}^{es})/max(\tau_j = 1..n)$)

7.2. Identified dynamic model

After the active candidate functions are determined in the first step of the algorithm, the iterative part starts by setting an initial value for σ_0. In this study, different initial values including 1e3, 5e3, 10e3, 50e3 and 100e3 are examined and the lowest error is obtained for σ_0 =10e3. In Fig. 9, the evolution of the relative torque prediction error (i.e. $E_\tau / \|\tau\|$), ξ_u, σ_0, σ_1, and Ω_s over each outer-loop iteration is presented for model A. Convergence after about 10 iterations is obvious from this figure. Moreover, ξ_u converges to unity which, as discussed in section 4, is necessary to ensure the accuracy of the algorithm. The results obtained for model B are presented in Fig. 10, showing a faster convergence. The relative error in torque prediction is close to the result of model A, while σ_0 and σ_1 are somewhat smaller compared to model A.

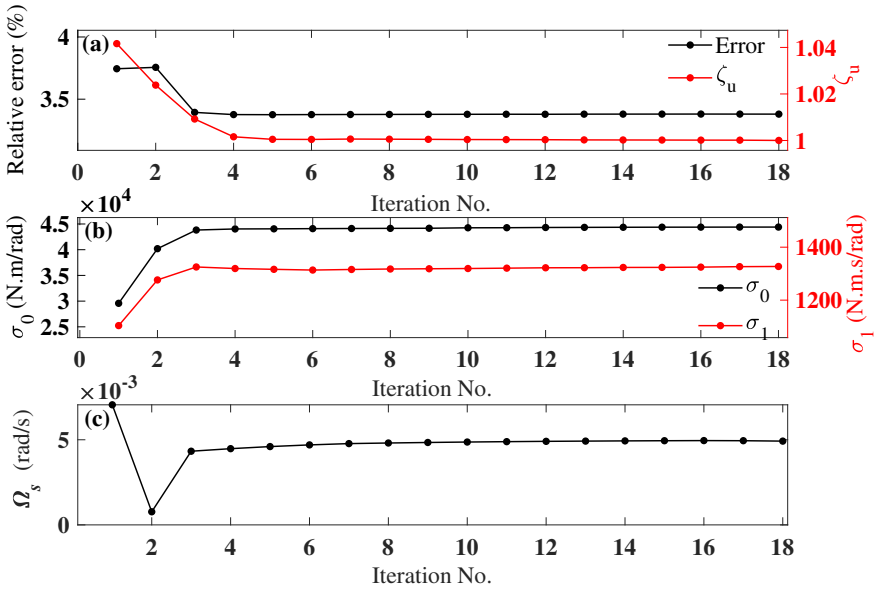

Figure 9: Variation of the results calculated through each outer-loop iteration of the proposed algorithm including (a) relative error in τ ($E_\tau/||\tau||$) and ξ_u, (b) σ_0 and σ_1, (c) Stribeck velocity, Ω_s

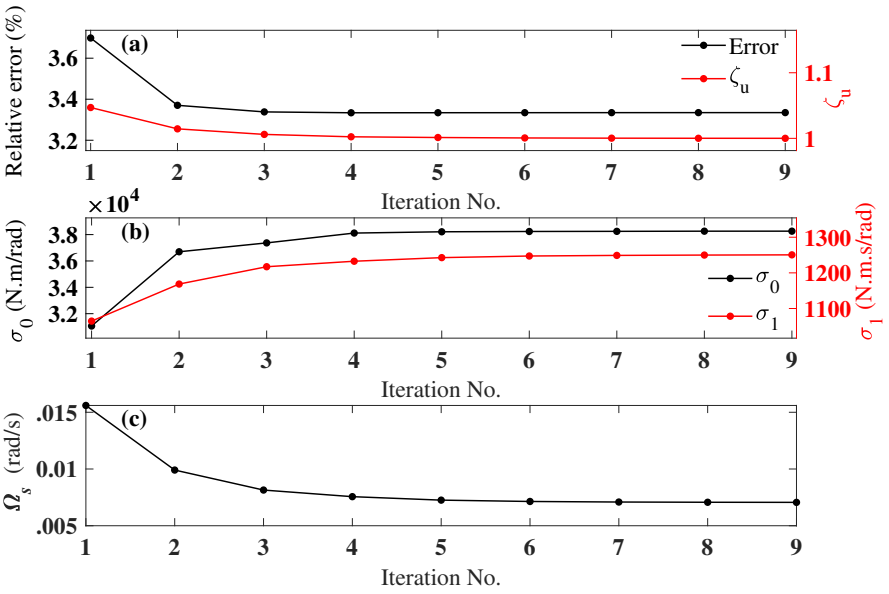

Figure 10: Variation of the results calculated through each outer-loop iteration of the proposed algorithm with model B (sign($\dot{q}$) is replaced with tanh($K\dot{q}$)) for (a) relative error in τ ($E_\tau/||\tau||$) and ξ_u, (b) σ_0 and σ_1, (c) Stribeck velocity, Ω_s

The rotor torque estimated by the identified model A for the training data sets 1 and 2 are shown in Fig. 11(a1) and (a2). Aside from small discrepancies near torque reversal points, a good agreement is observed between measured and estimated torques. The observed discrepancies can be attributed to the effect of stiction at those points. The corresponding relative torque prediction errors are also shown in Fig. 11(b1 and b2); the results obtained by the static model are also included for comparison. The considerably smaller errors that are obtained by the dynamic model at velocity zero-crossing points highlight the advantage of the identified dynamic model. Similar results are obtained in Fig. 12 for the test data sets 1 and 2, confirming the generalizability of the identified model.

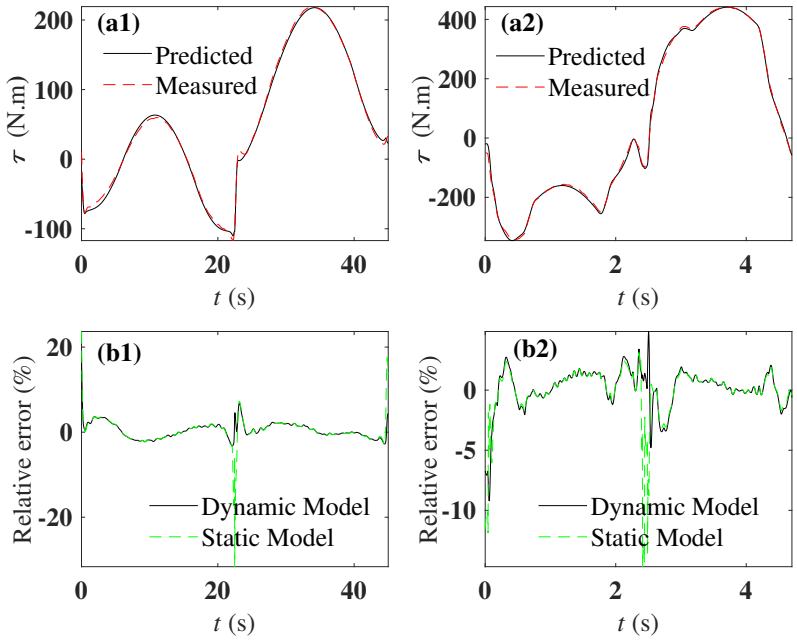

Figure 11: (a1),(a2): Comparison of the rotor torque estimated using the dynamic model A with the measured training data sets 1 and 2 (b1),(b2): time evolution of the relative error, $(\tau_j - {\tau_j}^{es})/max(\tau_j = 1..n)$, obtained by the dynamic and static models for the training data sets 1 and 2

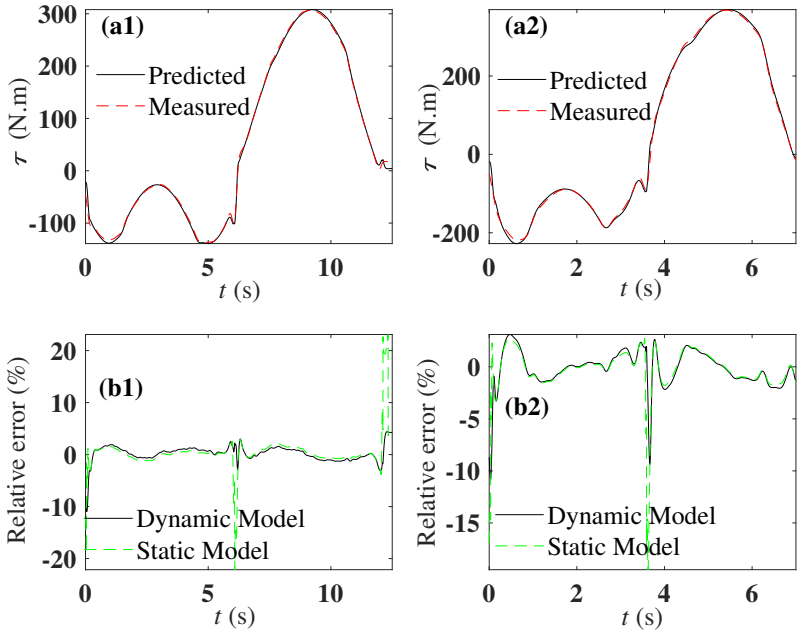

Figure 12: (a1),(a2): Comparison of the rotor torque estimated using the dynamic model A with the measured test data sets 1 and 2 (b1),(b2): time evolution of the relative error, obtained by the dynamic and static models for the test data sets 1 and 2

The measured time histories of the rotation angle, q, in test datasets 1 and 2 are compared with those obtained by solving the identified equation of motion. The results are shown in Figs. 13(a1) and (a2), where the predicted rotation angles coincide very well with the experimental result. The results for $\dot{q}$ are also presented in Figs.13(b1) and (b2). Aside from some larger differences at the constant velocity regions, the calculated velocities are close to the measured ones.

A similar analysis using model B led to torque predictions that would be indistinguishable from those obtained from model A; therefore, the results are not shown here. However, larger differences were observed in predicting the joint motion. This is illustrated in Fig. 14 which shows the time evolution of the relative errors in predicting q and $\dot{q}$. The relative error was obtained by using the relations, $(X_j - X_j{}^{es})/\max(X_j = 1..n)$ with X being substituted with q for the rotation angle in Fig. 14(a1) and (a2), and with $\dot{q}$ for the angular velocity in Fig. 14(b1) and (b2). According to this figure, model A has a slightly better performance at the time instants close to the stopping point, while model B performs better at points prior to motion reversal.

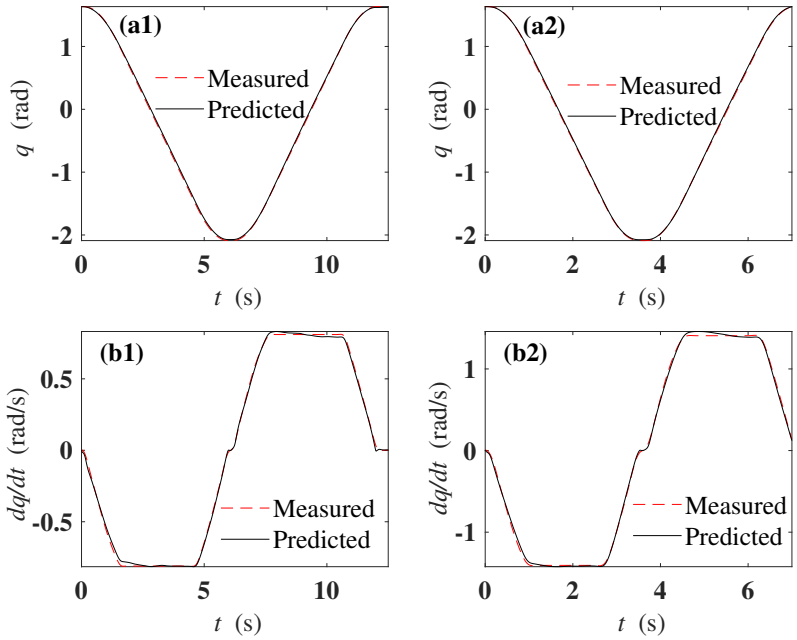

Figure 13: Comparison of the response estimated using the dynamic model A with the measured test data sets 1 and 2 for (a1),(a2): angular position of the robot link (b1),(b2) angular velocity of the robot link

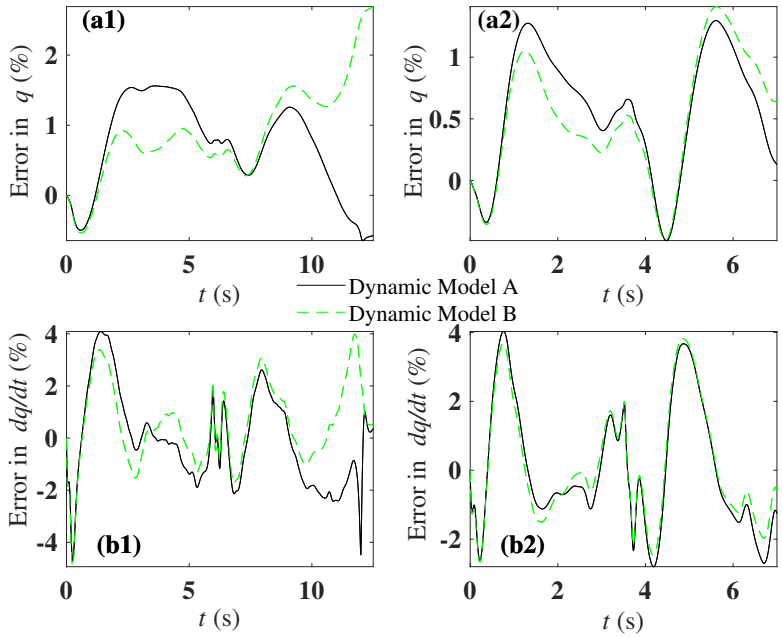

Figure 14: Comparison of the time evolution of the response relative error, estimated using the dynamic models A and B for (a1),(a2): angular position in test data sets 1 and 2 (b1),(b2): angular velocity in test data sets 1 and 2

7.3. Modified friction-velocity curves

The friction-velocity curves obtained from the static friction model in Fig.7 are modified in this section based on the identified dynamic model. Two different modified friction-velocity curves are obtained as a result. The first one is the result of directly applying the dynamic model to a specific trajectory. The training dataset 1 is used to compute this curve, which is limited to lower velocities and more influenced by stiction at velocity zero-crossing points. The curve is shown in Fig. 15(a) and (b), for models A and B, respectively. The curve is computed for acceleration and deceleration separately. A larger local peak is seen in the deceleration curve, which is unexpected because the break-away torque in the acceleration phase is expected to be larger than in deceleration. Although this observation is not commonly reported in the literature, it is still possible, as the theoretical and experimental results in [1] show.

The second modified friction-velocity curve, shown in Fig. 15, is computed by setting $\dot{z} = 0$ in the dynamic LuGre model in Eq. (6). Therefore, the relation used for computing this curve is the same as the static friction model used in the first step of the algorithm, with the difference that its parameters are updated during the iterative process of the algorithm. Figure 15 also includes the curves obtained by CVEs and the first approximation of the static model presented in section 7.1. The result shows that the curve corresponding to the dynamic

model with $\dot{z} = 0$ has smaller differences with the CVE-based curve at low velocities compared to the first approximation of the static model. This is in fact more pronounced in model A where the local peak is almost coincident with the result of the CVE. It is also seen in model B that the updated static model estimates the break-away torque (the torque at the local peak) about 6 percent higher than the CVE, while the first approximation of the static model estimates it about 15 percent lower than the CVE. Considering that CVEs describe static friction more accurately, it can be inferred that the identified friction model is improved significantly by the iterative steps in the proposed algorithm. The comparison of the two branches computed by the dynamic model also shows that the branch corresponding to the deceleration phase is closer to the result of CVEs, while the branch of the acceleration phase is more like the result of the static model identified in the first step of the algorithm.

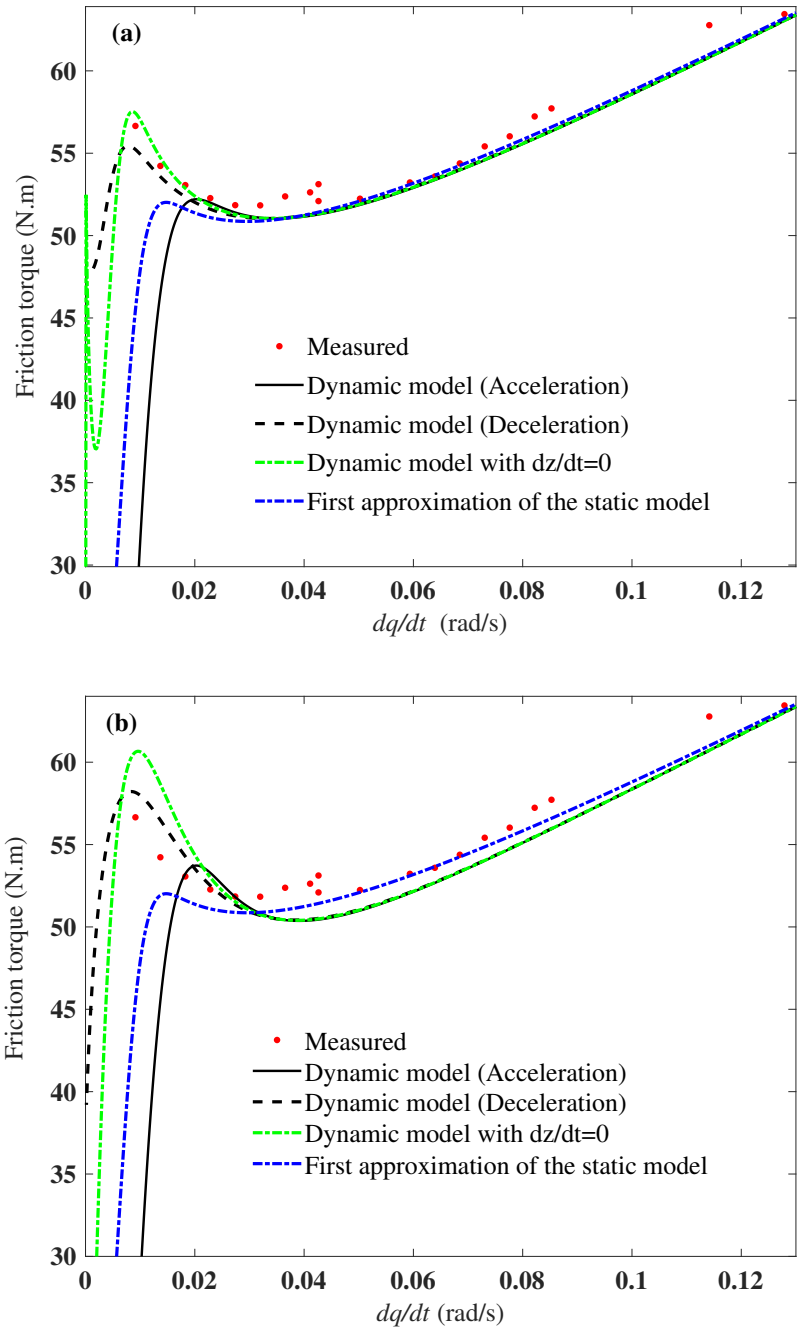

Figure 15: The friction-velocity curves obtained by the dynamic model in the accelerating and decelerating motions using the training data set 1, compared with the results of CVEs, the result of the dynamic model with $\dot{z} = 0$ and also the result of the first approximation of the static model. (a) model A (b) model B (sign($\dot{q}$) is replaced with tanh($K\dot{q}$))

8. Summary and conclusion

A new least-square based iterative algorithm was proposed for identifying the LuGre friction model parameters. SINDy-SR3 was employed in the first step to determine the most effective functions for modelling the nonlinear viscous friction and Stribeck effect in the static model. The result was then used in the iterative second and third steps of the algorithm to estimate the dynamic parameters and modify the static parameters. The application of the presented algorithm to a single joint of an industrial robot showed that the algorithm is capable of identifying the entire equation of motion in one experiment. Comparison against the velocity-friction curves obtained by CVEs also showed that the identified dynamic model performs similar to CVEs in the decelerating phase of motion.

Overall, the proposed algorithm was found to have the following desirable properties that can make it a suitable choice for estimating the parameters of joint models:

- The method can simultaneously estimate the inertial and friction properties together.
- The method can identify the static model based on a response-input time history rather than the time-consuming closed-loop CVEs.
- The static friction model is refined together with the dynamic model during the iterations.
- Since the optimization problems in this method are primarily based on the LSQM, the run-time of the process is not high. For instance, in the presented experimental case study, the model parameters were identified in about five minutes using a consumer-grade computer. Moreover, there are only two parameters that need to be assigned initial values at the beginning of the process.

Acknowledgement

Funding for this research was provided by the National Research Council Canada under grant DHGA-108-1.

References

[1] F. Al-Bender, V. Lampaert, J. Swevers, Modeling of dry sliding friction dynamics: From heuristic models to physically motivated models and back, Chaos: An Interdisciplinary Journal of Nonlinear Science 14 (2) (2004) 446–460.

[2] F. Al-Bender, V. Lampaert, J. Swevers, A novel generic model at asperity level for dry friction force dynamics, Tribology Letters 16 (2004) 81–93.

[3] M. Ruderman, T. Bertram, Two-state dynamic friction model with elasto-plasticity, Mechanical Systems and Signal Processing 39 (1-2) (2013) 316–332.

[4] F. Marques, P. Flores, J. P. Claro, H. M. Lankarani, Modeling and analysis of friction including rolling effects in multibody dynamics: a review, Multibody System Dynamics 45 (2019) 223–244.

[5] J. Wojewoda, A. Stefański, M. Wiercigroch, T. Kapitaniak, Hysteretic effects of dry friction: modelling and experimental studies, Philosophical Transactions of the Royal Society A: Mathematical, Physical and Engineering Sciences 366 (1866) (2008) 747–765.

[6] B. Armstrong-Hélouvry, P. Dupont, C. C. De Wit, A survey of models, analysis tools and compensation methods for the control of machines with friction, Automatica 30 (7) (1994) 1083–1138.

[7] A. C. Bittencourt, E. Wernholt, S. Sander-Tavallaey, T. Brogårdh, An extended friction model to capture load and temperature effects in robot joints, in: 2010 IEEE/RSJ international conference on intelligent robots and systems, IEEE, 2010, pp. 6161–6167.

[8] L. Gao, J. Yuan, Z. Han, S. Wang, N. Wang, A friction model with velocity, temperature and load torque effects for collaborative industrial robot joints, in: 2017 IEEE/RSJ international conference on intelligent robots and systems (IROS), IEEE, 2017, pp. 3027–3032.

[9] H. Liao, S. Fan, D. Fan, Friction compensation of harmonic gear based on location relationship, Proceedings of the Institution of Mechanical Engineers, Part I: Journal of Systems and Control Engineering 230 (8) (2016) 695–705.

[10] M. N. Nevmerzhitskiy, B. S. Notkin, A. V. Vara, K. V. Zmeu, et al., Friction model of industrial robot joint with temperature correction by example of kuka kr10, Journal of Robotics 2019 (2019).

[11] B. Armstrong-Helouvry, Control of machines with friction, Vol. 128, Springer Science & Business Media, 2012.

[12] M. Indri, I. Lazzero, A. Antoniazza, A. M. Bottero, Friction modeling and identification for industrial manipulators, in: 2013 IEEE 18th conference on emerging technologies & factory automation (ETFA), IEEE, 2013, pp. 1–8.

[13] X. Wang, S. Wang, High performance adaptive control of mechanical servo system with lugre friction model: identification and compensation (2012).

[14] R. Hensen, G. Z. Angelis, M. Van de Molengraft, A. De Jager, J. Kok, Grey-box modeling of friction: An experimental case-study, European Journal of Control 6 (3) (2000) 258–267.

[15] J. Fehr, A. Kargl, H. Eschmann, Identification of friction models for mpc-based control of a powercube serial robot, arXiv preprint arXiv:2203.10896 (2022).

[16] S. L. Brunton, J. L. Proctor, J. N. Kutz, Discovering governing equations from data by sparse identification of nonlinear dynamical systems, Proceedings of the national academy of sciences 113 (15) (2016) 3932–3937.

[17] E. Kaiser, J. N. Kutz, S. L. Brunton, Sparse identification of nonlinear dynamics for model predictive control in the low-data limit, Proceedings of the Royal Society A 474 (2219) (2018) 20180335.

[18] C. C. De Wit, H. Olsson, K. J. Astrom, P. Lischinsky, A new model for control of systems with friction, IEEE Transactions on automatic control 40 (3) (1995) 419–425.

[19] F. Marques, Ł. Woliński, M. Wojtyra, P. Flores, H. M. Lankarani, An investigation of a novel lugre-based friction force model, Mechanism and Machine Theory 166 (2021) 104493.

[20] P. R. Dahl, A solid friction model, Tech. rep., Aerospace Corp El Segundo Ca (1968).

[21] J. Swevers, F. Al-Bender, C. G. Ganseman, T. Projogo, An integrated friction model structure with improved presliding behavior for accurate friction compensation, IEEE Transactions on automatic control 45 (4) (2000) 675–686.

[22] F. Al-Bender, V. Lampaert, J. Swevers, The generalized maxwell-slip model: a novel model for friction simulation and compensation, IEEE Transactions on automatic control 50 (11) (2005) 1883–1887.

[23] P. Dupont, V. Hayward, B. Armstrong, F. Altpeter, Single state elastoplastic friction models, IEEE Transactions on automatic control 47 (5) (2002) 787–792.

[24] V. Lampaert, J. Swevers, F. Al-Bender, Modification of the leuven integrated friction model structure, IEEE transactions on Automatic Control 47 (4) (2002) 683–687.

[25] M. Indri, S. Trapani, Framework for static and dynamic friction identification for industrial manipulators, IEEE/ASME Transactions on Mechatronics 25 (3) (2020) 1589–1599.

[26] X. Wang, S. Lin, S. Wang, Dynamic friction parameter identification method with lugre model for direct-drive rotary torque motor, Mathematical Problems in Engineering 2016 (2016).

[27] T. Xi, T. Fujita, S. Kehne, R. Ikeda, M. Fey, C. Brecher, An extended lugre model for estimating nonlinear frictions in feed drive systems of machine tools, Procedia CIRP 107 (2022) 452–457.

[28] Z. Zhou, X. Zheng, Q. Wang, Z. Chen, Y. Sun, B. Liang, Modeling and simulation of point contact multibody system dynamics based on the 2d lugre friction model, Mechanism and Machine Theory 158 (2021) 104244.

[29] C. C. De Wit, P. Lischinsky, Adaptive friction compensation with partially known dynamic friction model, International journal of adaptive control and signal processing 11 (1) (1997) 65–80.

[30] F. Altpeter, P. Myszkorowski, R. Longchamp, Identification for control of drives with friction, IFAC Proceedings Volumes 30 (6) (1997) 529–533.

[31] P. S. Gandhi, F. H. Ghorbel, J. Dabney, Modeling, identification, and compensation of friction in harmonic drives, in: Proceedings of the 41st IEEE Conference on Decision and Control, 2002., Vol. 1, IEEE, 2002, pp. 160–166.

[32] R. H. Hensen, M. J. van de Molengraft, M. Steinbuch, Frequency domain identification of dynamic friction model parameters, IEEE Transactions on Control Systems Technology 10 (2) (2002) 191–196.

[33] D. D. Rizos, S. D. Fassois, Friction identification based upon the lugre and maxwell slip models, IEEE Transactions on Control Systems Technology 17 (1) (2008) 153–160.

[34] K. Worden, C. Wong, U. Parlitz, A. Hornstein, D. Engster, T. Tjahjowidodo, F. Al-Bender, D. Rizos, S. Fassois, Identification of pre-sliding and sliding friction dynamics: Grey box and black-box models, Mechanical systems and signal Processing 21 (1) (2007) 514–534.

[35] S.-J. Huang, C.-M. Chiu, Optimal lugre friction model identification based on genetic algorithm and sliding mode control of a piezoelectric-actuating table, Transactions of the Institute of Measurement and Control 31 (2) (2009) 181–203.

[36] T. Liang, C. Qiang, N. Yurong, Y. Suhua, S. Guofa, Adaptive control of mechanical servo system with glowworm swarm friction identification, in: 2015 34th Chinese Control Conference (CCC), IEEE, 2015, pp. 3132–3138.

[37] Y. Yu, Y. Li, J. Li, Parameter identification and sensitivity analysis of an improved lugre friction model for magnetorheological elastomer base isolator, Meccanica 50 (2015) 2691–2707.

[38] P. Feyel, G. Duc, G. Sandou, Lugre friction model identification and compensator tuning using a differential evolution algorithm, in: 2013 IEEE Symposium on Differential Evolution (SDE), IEEE, 2013, pp. 85–91.

[39] Z. Ping, W. Zhang, Y. Fu, Improved lugre-based friction modeling of the electric linear load simulator, in: Journal of Physics: Conference Series, Vol. 2338, IOP Publishing, 2022, p. 012079.

[40] A. Janot, P. O. Vandanjon, M. Gautier, An instrumental variable approach for rigid industrial robots identification, Control Engineering Practice 25 (2014) 85–101.

[41] D. Kostic, B. De Jager, M. Steinbuch, R. Hensen, Modeling and identification for high-performance robot control: An rrr-robotic arm case study, IEEE Transactions on Control Systems Technology 12 (6) (2004) 904–919.

[42] J. Swevers, C. Ganseman, J. De Schutter, H. Van Brussel, Experimental robot identification using optimised periodic trajectories, Mechanical Systems and Signal Processing 10 (5) (1996) 561–577.

[43] P. Zheng, T. Askham, S. L. Brunton, J. N. Kutz, A. Y. Aravkin, A unified framework for sparse relaxed regularized regression: Sr3, IEEE Access 7 (2018) 1404–1423.

[44] K. Champion, P. Zheng, A. Y. Aravkin, S. L. Brunton, J. N. Kutz, A unified sparse optimization framework to learn parsimonious physics-informed models from data, IEEE Access 8 (2020) 169259–169271.

[45] J. B. Jonker, R. Waiboer, R. Aarts, Modelling of joint friction in robotic manipulators with gear transmissions, in: Multibody Dynamics, Springer, 2007, pp. 221–243.

[46] N. M. Mangan, S. L. Brunton, J. L. Proctor, J. N. Kutz, Inferring biological networks by sparse identification of nonlinear dynamics, IEEE Transactions on Molecular, Biological and Multi-Scale Communications 2 (1) (2016) 52–63.

[47] K. Kaheman, J. N. Kutz, S. L. Brunton, Sindy-pi: a robust algorithm for parallel implicit sparse identification of nonlinear dynamics, Proceedings of the Royal Society A 476 (2242) (2020) 20200279.

[48] L. I. Rudin, S. Osher, E. Fatemi, Nonlinear total variation based noise removal algorithms, Physica D: nonlinear phenomena 60 (1-4) (1992) 259–268.

[49] R. Chartrand, Numerical differentiation of noisy, nonsmooth data, International Scholarly Research Notices 2011 (2011).

[50] M. Stender, S. Oberst, N. Hoffmann, Recovery of differential equations from impulse response time series data for model identification and feature extraction, Vibration 2 (1) (2019) 25–46.

[51] N. M. Mangan, J. N. Kutz, S. L. Brunton, J. L. Proctor, Model selection for dynamical systems via sparse regression and information criteria, Proceedings of the Royal Society A: Mathematical, Physical and Engineering Sciences 473 (2204) (2017) 20170009.